Influence of nanocrystal concentration on the performance of hybrid P3HT:TBPO-capped CdSe nanocrystal solar cells

A. Benchaabane[1,2] · **Z. Ben Hamed**[2] · **M. A. Sanhoury**[3] · **F. Kouki**[2] ·
A. Zeinert[1] · **H. Bouchriha**[2]

Abstract Hybrid solar cells based on the polymer poly(3-hexylthiophene) (P3HT) and colloidal TBPO-capped CdSe nanocrystals (NCs) have been studied using varying amounts of CdSe NCs. The power conversion efficiency of these devices increased monotonically from $\eta_p = 0.05$ % for 0 wt% NCs under white light illumination to 0.25 % for 40 wt% and then decreased to 0.07 % for 60 wt% NCs. The improvement in efficiency was mainly due to a remarkable increase in both the short-circuit current and open-circuit voltage, whereas the fill factor was less affected. In addition, the PL spectra of these devices showed a significant quenching suggesting rapid charge or energy transfer at the polymer–nanocrystal interface. The results indicate that capping with the smaller TBPO ligand did not considerably passivate the CdSe nanocrystal surface and the improvement in device performance could be mainly due to a pronounced PL quenching. The effect of using a relatively small TBPO compared to the commonly used TOPO ligand on the performance of these devices is discussed.

✉ A. Benchaabane
benchaabane.aida@yahoo.fr

[1] Laboratoire de Physique de la Matière Condensée, Faculté des Sciences d'Amiens, 80039 Amiens, France

[2] Laboratoire Matériaux avancés et phénomènes quantiques, Faculté des Sciences de Tunis El Manar, Université Tunis El-Manar, Campus Universitaire, 2092 Tunis, Tunisia

[3] Laboratoire de Chimie Organique Structurale, Synthèse et Etudes Physicochimiques, Université Tunis-El Manar, Campus Universitaire, 2092 Tunis, Tunisia

1 Introduction

In the past few decades, organic materials based on small molecular weight organic compounds and conjugated polymers have attracted considerable attention due to their advantages of low cost, light weight and flexibility on plastic substrates [1–8]. On the other hand, inorganic nanocrystals (NCs) or quantum dots such as CdSe, CdS or ZnS belonging to the II–IV direct band gap group of semiconductors are characterized by a large confinement of electrons and holes at nanometer scale and have a narrow spectrum of emission and high quantum yield luminescence. The Wannier-Mott excitons created by light absorption in inorganic semiconductors have a much larger Bohr radius than the Frenkel excitons occurring in organic semiconductors [9–11]. In the former case, the photogenerated geminate hole–electron pairs could be more easily separated by an external electric field.

The incorporation of NCs in the polymer matrix allows an inexpensively solution processing of the hybrid organic–inorganic device. This combines the diversity of conjugated polymers with the best electronic and optical properties of inorganic semiconductor NCs by a resonant transfer of energy through formation of hybrid excitons having properties of both types of excitons (Frenkel and Wannier) which are very sensitive to the external perturbation of the electric field in the heterostructure. The dependence of the transfer on the energy gaps of both the polymer and the nanocrystal is now well known and has been thoroughly investigated [12–16]. These hybrid systems are promising devices with better conversion efficiencies [17]. Therefore, several works using inorganic NCs incorporated in poly(3-hexylthiophene) (P3HT) have been investigated. For example, Zhou et al. [18] reported on bulk-heterojunction hybrid solar cells based on blends

of non-ligand-exchanged CdSe NCs and P3HT with power conversion efficiencies of about 2 %.

Ligand exchange with small molecules such as pyridine is a common process used to remove large and insulating organic ligands employed during the preparation of inorganic NCs in order to better facilitate charge transfer between the donor and acceptor and also to enhance charge collection from the NC phase [19–26]. More recently, it has been shown that surface ligands can potentially contribute to the HOMO/LUMO energies of the semiconductor NCs. This could affect considerably the device performance since V_{oc} was reported to be directly proportional to the difference in energy (ΔE) between the HOMO of the donor polymer and the LUMO of the NC acceptor [27].

In this paper, inorganic CdSe NCs capped with tributylphosphine oxide (TBPO) as a surfactant ligand are blended with P3HT. Hybrid nanocomposites formed with different TBPO-capped CdSe concentrations were prepared and characterized. Both materials and devices are studied and optimized with respect to NC concentration through investigation of their structural, optical, electronic and energetic properties.

2 Experimental

2.1 Synthesis of CdSe NCs

Cadmium selenide NCs were prepared following literature methods [28] with some modifications using tributylphosphine instead of trioctylphosphine derivatives in order to reduce the bulkiness of the capping agent; to a solution of cadmium acetate (3 mmol, 0.79 g) in tributylphosphine oxide (TBPO; 15 mmol, 3.27 g) was added dropwise a solution of tributylphosphine selenide (2.1 mmol, 5.9 g) in tributylphosphine (TBP) (5 ml). The reaction mixture was heated at 95–105 °C overnight. After cooling to room temperature (about 25 °C), methanol was added to the red suspension obtained to cause further precipitation. The suspension was centrifuged three times at 4000 rpm for 30 min followed by washing with hexane and drying in an oven to obtain CdSe as deep red powder.

2.2 P3HT:% CdSe film and device fabrication

P3HT (Sigma Aldrich) was dissolved in chloroform (0.1 g/ml), and the solution was stirred for 4 h at room temperature. The composite solution was then prepared by adding CdSe NCs (as synthesized by above procedure) to the P3HT solution. In keeping a fixed concentration of P3HT, four different nanocomposites corresponding to the concentration 0 (pure polymer), 20, 40 and 60 wt% of CdSe were prepared. The solutions were stirred in order to disperse the CdSe powder to prevent nanoparticle aggregation. First, the glass substrates were cleaned by ultrasonic treatment for 20 min in acetone followed by ethanol. After that, substrates were dried under a stream of argon. A filtered dispersion of polyethylenedioxythiophene doped with polystyrene sulfonic acid (PEDOT:PSS) in water, purchased from Sigma Aldrich, was then spin-coated onto cleaned ITO-glass substrates at a rate of 2000 rpm for 60 s, which were subsequently baked at 100 °C for 30 min to remove residual water. The suspension of the CdSe NCs and P3HT polymer in chloroform was spin-coated on top of the PEDOT:PSS thin film at 2000 rpm for 60 s to form a P3HT:CdSe photoactive layer of ∼200 nm thickness as shown in Fig. 7a. Then, all the samples were annealed at 80 °C for 120 min. Subsequently, samples were loaded into a vacuum deposition chamber (background pressure ≈ 10^{-6} Pa) to deposit 100-nm-thick aluminum cathode through a shadow mask (device area of 0.2 cm^2).

2.3 P3HT:% CdSe film and device characterization

The morphology of CdSe NCs was investigated by transmission electron microscope (TEM) (Technai G220, Fei Company) with an accelerating voltage of 200 kV.

The morphological structure of the P3HT:CdSe NC hybrid films were investigated by scanning electron microscope (SEM) (Canon with field effects, Philips XL30) and by atomic force microscopy (AFM) (Veeco metrology group Nanoscope III a Dimension 3100 controller) in the tapping mode. The absorption spectra of the samples on ITO/PEDOT:PSS substrates were recorded using a Perkin Elmer Lambda 950 UV–Vis spectrophotometer. The photoluminescence (PL) spectra were recorded on a Perkin Elmer MPF-644B spectrofluorometer at a wave excitation of 307 nm. The current density–voltage (J–V) curves were measured at room temperature in the dark and under illumination using a Keithley 2400 source meter connected to the electrodes (ITO and Al) and controlled by a computer. The photovoltaic characteristics are performed under illumination of the cell on ITO side through an optical quartz fiber and by a halogen tungsten lamp. The input power of the white is about 10 mW/cm^2.
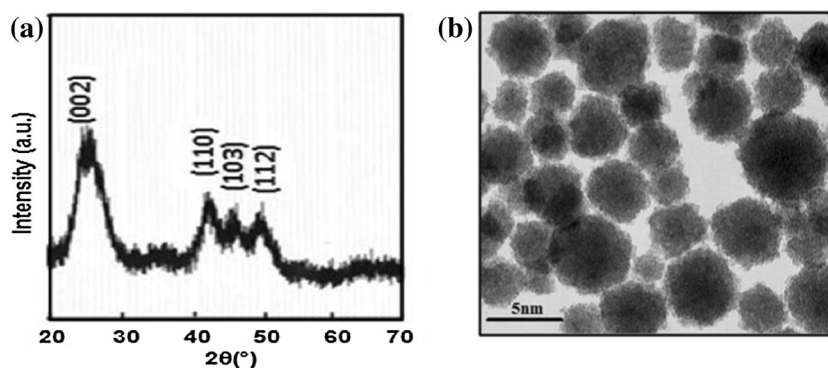
3 Results and discussion

3.1 Nanocrystal size and optical characterization

3.1.1 Nanocrystal size

The size of the synthesized CdSe NCs was also confirmed by TEM analysis shown in Fig. 1a which reveals that the nanoparticle diameter is about 4 nm. The powder XRD

Fig. 1 TEM images **a** and powder XRD pattern **b** of TBPO-capped CdSe NCs

pattern (Fig. 1b) gave very broad peaks at $2\theta = 25.2°$, 41.9°, 46.0° and 49.7° which can be assigned to a wurtzite hexagonal CdSe phase. This is confirmed by the significant intensity at 46° which is consistent with (1 0 3) diffraction lines for the hexagonal phase. The breadth of the peaks suggested that the nanocrystal size was very small. The application of the Sherrer equation gives an estimate of the nanocrystal size of 3.7 nm which is in the same order of those determined above. It can therefore be assumed that the averaged size of the NCs is 3.4 ± 0.3 nm.

3.1.2 Optical characterization

CdSe NC optical properties were investigated in the UV–Visible range by optical absorption spectroscopy and PL. The PL spectrum exhibits a maximum at 625 nm, and the absorption spectrum shows two main absorption peaks at 340 and 550 nm (Fig. 2).

The optical band gap (E_g) of CdSe NCs could be determined with the Tauc relation [29] using the absorption spectrum. For instance, the band gap of these NCs as estimated from their absorption onset is about 1.95 eV which is greater than that of bulk CdSe (1.74 eV) [30, 31], showing a blue shift of 0.21 eV. This effect is accounted
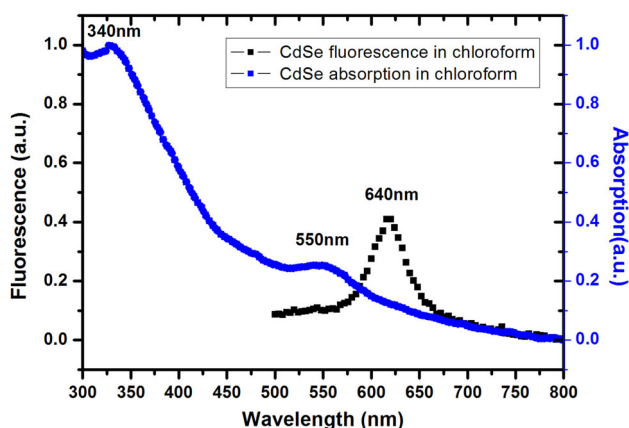
for by the size quantization in nanocrystalline semiconductors [32], due to the strong confinement of holes and electrons in the NCs.

3.2 Structural characterization of P3HT:% CdSe films

Figure 3 shows the SEM images of the surface of active layers with P3HT:CdSe loading amount of 0, 20, 40 and 60 %. Figure 3a reveals that the surface of active layer of pure polymer is porous. When the loading amount was subsequently increased, however, the surface roughness increases. SEM image of P3HT thin film at 40 % CdSe NCs (Fig. 3c) shows that the surface of active layer is quite smooth at this concentration with best dispersion of NCs in the polymer matrix and there is no observed aggregation of CdSe, while in the case of the higher CdSe amount (60 %) (Fig. 3d), the surface roughness becomes worse and the probability of NCs aggregation is higher, leading to small contact surface in P3HT:CdSe. This would suggest that the best device would be that with 40 %wt CdSe since it offers the highest interface area in such a bulk-heterojunction structure.

The effect of CdSe nanocrystal concentration on the device performance was also structurally characterized by thin-film AFM morphological analysis (Fig. 4) which revealed that the interpenetrating network structure is established for the 40 % sample, giving the best monodispersed device, while the film with 60 % CdSe results in the formation of aggregates. It is well known that grain sizes and grain distributions strongly influence the performance of photovoltaic devices [33].

3.3 Optical characterization of P3HT:% CdSe films

This energy transfer leads to the formation of excitons in CdSe NCs. At the same time, hole transfer from nanoparticle to P3HT polymer could take place. Next, some part of lower energy exciton is formed in CdSe, and then, free charge carriers are generated by hole transfer from HOMO of CdSe NCs to the HOMO of P3HT.

Fig. 2 UV–Vis and PL spectra of TBPO-capped CdSe NCs

Fig. 3 SEM images of
a P3HT:0 % CdSe,
b P3HT:20 % CdSe,
c P3HT:40 % CdSe and
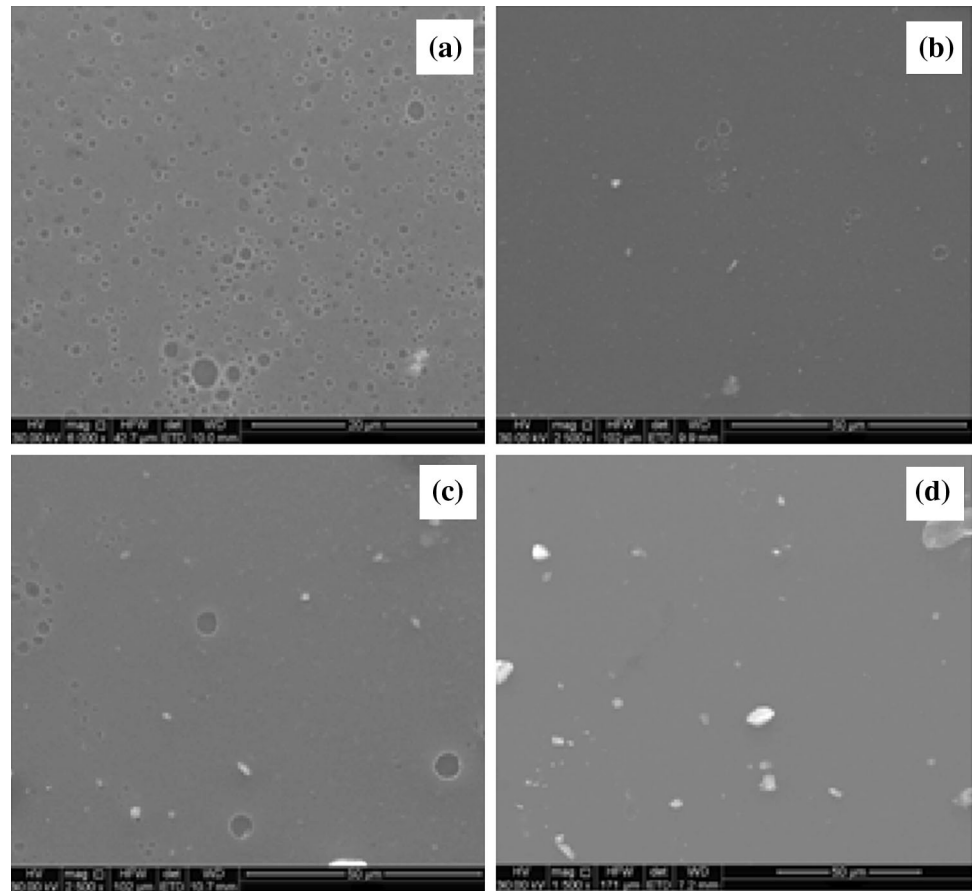**d** P3HT:60 % CdSe thin films

Fig. 4 AFM images of
a P3HT:0 % CdSe,
b P3HT:20 % CdSe,
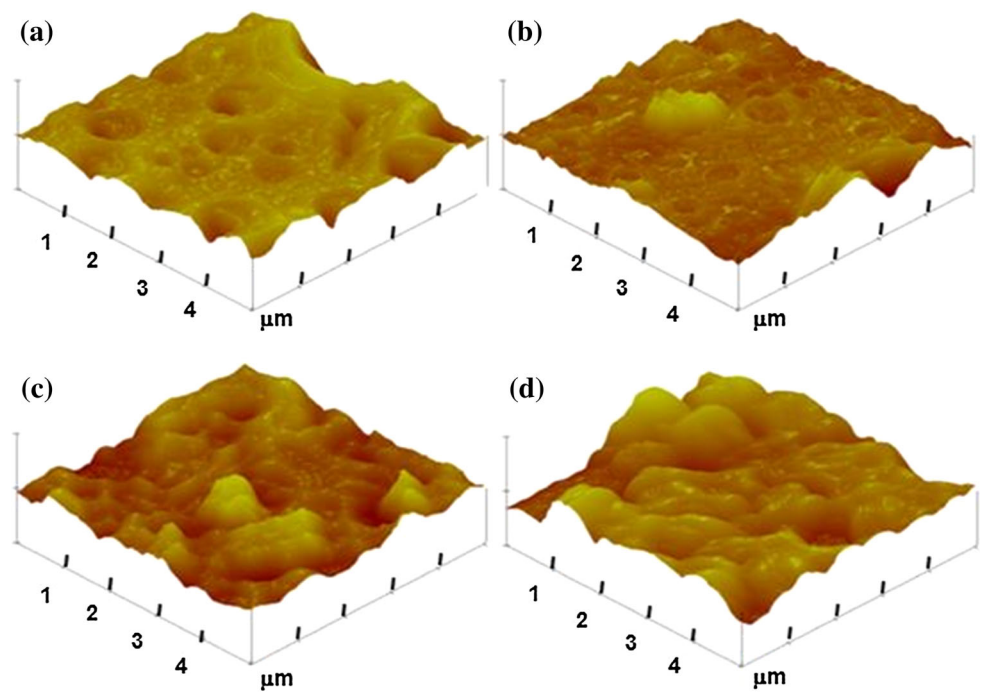**c** P3HT:40 % CdSe,
d P3HT:60 % CdSe thin films

Figure 5 shows the UV–Vis and PL intensity profiles of P3HT:CdSe composites as a function of CdSe nanocrystal concentrations in chloroform solutions and in solid thin films. As can be seen, the variation of NCs concentration shows nearly no change in the UV absorption intensities (Fig. 5a), while the PL intensity decreases gradually from pure P3HT until 40 wt% CdSe and then decreases slightly for 60 % device (Fig. 5b, c). This confirms that the 40 % device leads to the strongest quenching of the PL intensity, again in good agreement with the structural results. The quenching phenomenon indicates that more excited electrons decayed via non-radiative transitions which could be attributed to a significant charge and/or energy transfer from P3HT to CdSe nanocrystal phases. It is worth to note that the PL quantum efficiency for P3HT:TBPO-CdSe 40 wt% is approximately 77 versus 67 % obtained for the same device fabricated with TOPO-capped CdSe and is comparable to that obtained with pyridine-capped CdSe [34, 35]. This is not surprising since the surface ligand TOPO is approximately two times bulkier than TBPO [36], leading to a less thick barrier between the nanocrystal core and the polymer.

Indeed, excitons are essentially created in the P3HT matrix through the photon absorption by this material. When they reach the polymer–nanocrystal interface, not only Förster resonance energy transfer (FRET) is expected but also charge transfer process can occur. These transfer processes could cause the formation of hybrid excitons. The dissociation of these hybrid excitons in the inorganic–organic interface occurs through three processes: (1) exciton formation in organic, followed by electron transfer to TOPO-capped CdSe; (2) exciton formation in organic, followed by energy transfer to TOPO-capped CdSe and then by hole transfer to organic; and (3) exciton formation in TOPO-capped CdSe, followed by hole transfer to organic, respectively [37, 38].

This means that the driving force for this interaction would be the strong dipole–dipole interaction between the Cd^{2+} ions on the surface of NCs and sulfur atoms of the polymer. In particular, the P3HT has a higher amount of sulfur atoms (from the thiophene rings) in the polymer chain available to interact more effectively with the CdSe NCs. Thus, interaction becomes more effective, which means that, if the immersion of the TBPO-capped CdSe
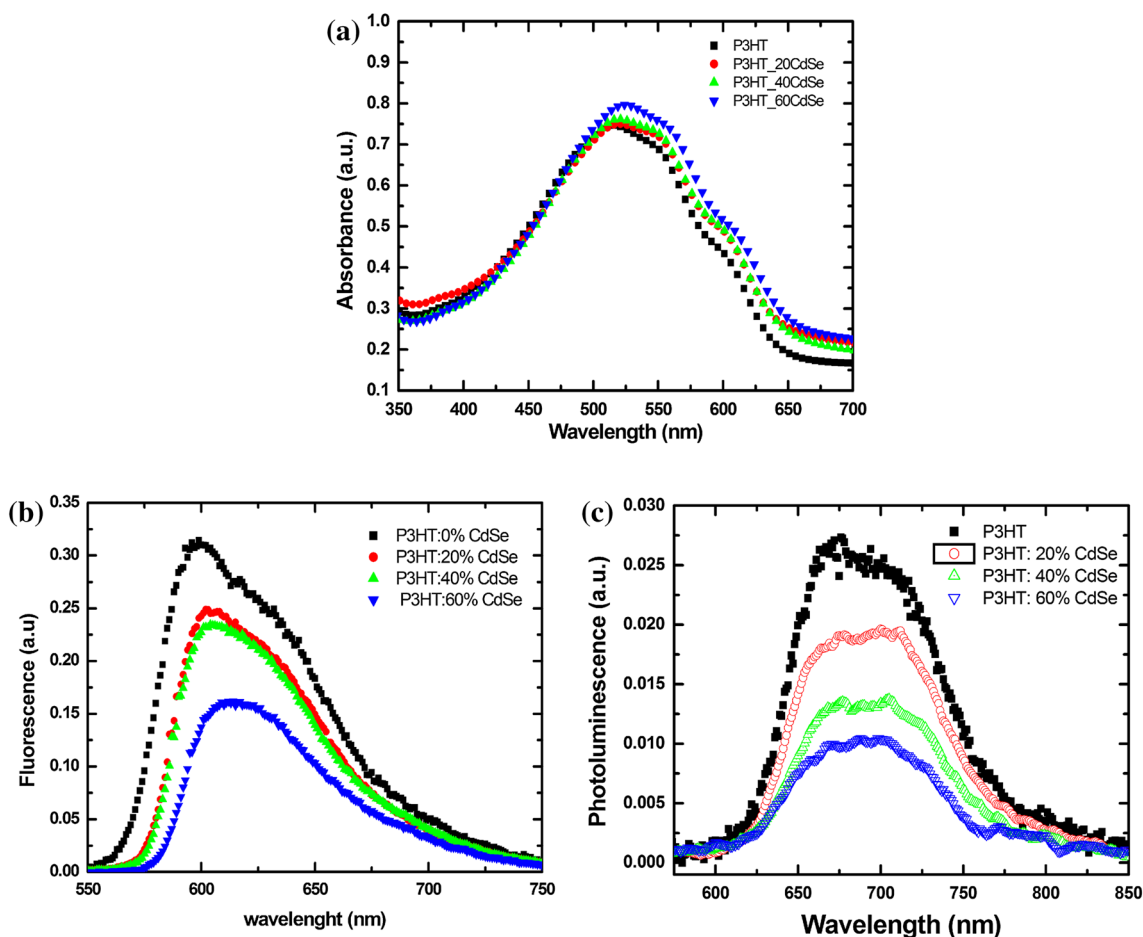

Fig. 5 Absorption **a** and emission (**b** in solution, **c** in solid thin films) intensity profiles of P3HT:CdSe composites as a function of CdSe concentration
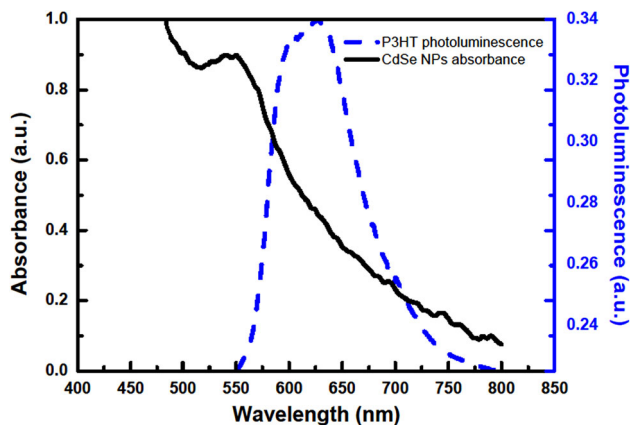
Fig. 6 Overlap of CdSe absorbance and P3HT fluorescence spectra

NCs in the film increases, molecular vibrations in the thiophene rings change their behavior. In other word, the NC's are physically doped in the polymer network [39].

The band gap of P3HT is near to that of CdSe, excitons are formed in the polymer, and when they reach the polymer–CdSe nanoparticle interface, a direct electron or exciton transfer occurs from polymer (donor material) to CdSe nanoparticle (acceptor material). The Förster resonance energy transfer (exciton transfer) is possible as shown by the spectral overlap between the emission spectrum of P3HT and absorption spectrum of the CdSe NCs (Fig. 6) [28].

3.4 Electrical characterizations

3.4.1 Effect of nanocrystal concentration on the performance of P3HT:CdSe devices

The composite solution was prepared by adding different concentration of TBPO-capped CdSe NCs (20, 40 and 60 wt%). Figure 7 shows the architecture and energy level diagram for P3HT:CdSe photovoltaic cell. Electron affinity and ionization potential could be estimated to be 4.2 and 6.1 eV, respectively. These values were based on

those of CdSe in the bulk and the relative shift of the conduction and valence band edges in the NCs due to confinement effect [40]. The energy level offsets at the interface between the inorganic and the organic phases of the nanocomposite ($\Delta E_{P3HT:CdSe}$) are about 1 eV. Such energy offsets would be sufficient to enable efficient dissociation of photogenerated excitons at the P3HT:CdSe interface.

3.4.2 Dark current

Figure 8 shows dark current characteristics as a function of applied voltage in the range (0–3 V) for pure P3HT and for P3HT:CdSe hybrid cells corresponding to 20, 40 and 60 wt% of CdSe nanoparticles. These characteristics define two operating ranges: At low voltage, we have the usual $J \propto V^m$ ($m \approx 2$) dependence of space-charge-limited current (SCLC) dominated by one type of traps; at high voltage, we have the dependence of $J \propto V^m$ ($9 < m < 12$) which is attributed to the trap-charge-limited current (TCLC). The voltage V_{TFL} corresponding to this trap field
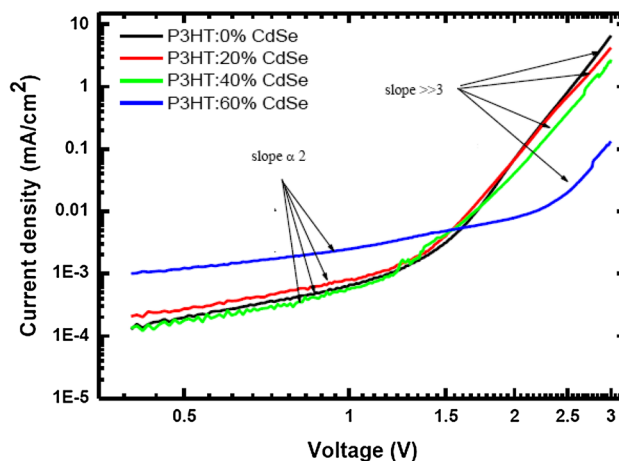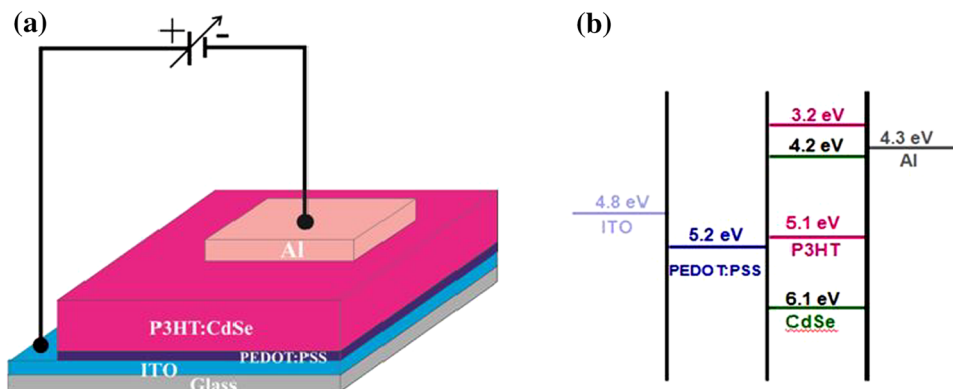

Fig. 8 Log–log current–voltage characteristics versus applied voltage

Fig. 7 Architecture **a** and diagram of energies referenced from vacuum level **b** for hybrid P3HT:CdSe solar cells

limit allows the evaluation of traps density by the relation [41] as shown in Fig. 10:

$$N_p = \frac{3}{2}\frac{\varepsilon}{e}\frac{V_{TFL}}{L^2}$$

where $\varepsilon = \varepsilon_0\varepsilon_r$ is the dielectric permittivity, where $\varepsilon_0 = 8.85.10^{-12}$ F/m is the vacuum permittivity and $\varepsilon_r = 3$ [42], 3.6 [43], 4 [43] and 6 [40] are the effective dielectric constants for 0, 20, 40 and 60 wt% of CdSe cells, respectively; e: the elementary charge; and $L = 200$ nm: the thickness of the active layer.

Table 1 summarizes the density of traps for the different concentrations. It seems for the low and middle concentrations that the density of traps is nearly constant, but for the highest concentration (60 % CdSe) this density is considerably increased, probably due to the creation of other defects in polymer by incorporation of a high density of nanoparticles. This would induce higher recombination rates of carriers [44].

By using a space-charge-limited current, it is possible to evaluate charge carrier mobility from the relation:

$$J = \frac{9}{8}\varepsilon_0\varepsilon_r\mu\frac{V^2}{d^3}$$

where ε_0 is the permittivity of free space, ε_r is the constant of the polymer, and μ is the effective mobility and d is the thickness of the active layer. The values of μ for the four concentrations are reported in Table 2. The mobility changes slightly for 20 and 40 wt% samples, while the 60 wt% CdSe device shows a sadden increase of up to 5 times that of pristine polymer. This could be explained by the absence of phase segregation in the latter device, in good agreement with the results reported for closely related materials [45]. However, a barrier at the interface due to a probable chemical reaction between the electrode and organic materials involving Schottky and/or Poole–Frenkel effects are not to be excluded.

The above results show that the variation of CdSe concentrations did not affect either the absorption of hybrid films or their electron mobility, but did affect the PL intensity. This could give more insights as to the mechanism of the performance improvement at the 40 wt% CdSe. We believe, therefore, that the main reason for this should be related to the quenching of the PL intensity upon increasing CdSe concentration in the blend.

Table 2 Photovoltaic device parameters of P3HT:% CdSe-based system

	V_{oc} (V)	J_{sc} (mA/cm^2)	FF	$\eta \times 10^{-1}$ (%)
P3HT:0 % CdSe	0.45	0.06	0.20	0.5
P3HT:20 % CdSe	0.72	0.12	0.18	1.5
P3HT:40 % CdSe	0.74	0.18	0.19	2.5
P3HT:60 % CdSe	0.34	0.09	0.22	0.7

3.4.3 Photovoltaic parameters

For evaluation of the device performance, the complete solar cell structure is glass/ITO/PEDOT:PSS/CdSe-P3HT/Al in which the CdSe NCs were capped with the TBPO ligand and their concentrations varied from 0 to 60 wt%. Current density voltage (J–V) curves of the devices were measured at room temperature in the dark and under white light illumination using different CdSe concentrations (Fig. 9). Figure 10 shows that the incorporation of CdSe NCs in the polymer matrix affects both the V_{oc} and J_{sc}. A comparison of the photovoltaic parameters and the performances of the pure and hybrid cells is shown in Table 2.

As shown in Table 2, both V_{oc} and J_{sc} increase with the concentration of NCs up to 40 % and decrease at 60 %. The device performance is sensitive to the NCs concentration, and the values of V_{oc} (0.35–0.75 V) are considerably affected by the NCs concentration and correspond to the expected maximum open-circuit voltage given by the difference in work function between ITO (4.7 eV) [28] and Al (4.3 eV) [46]. However, the fill factor is nearly constant (0.20). Figure 10c shows a tenfold increase in the power conversion efficiency η from the pure polymer to the 40 wt% hybrid cell and a sharp decrease beyond this value.

The above results show that the most pronounced dependence on the CdSe nanocrystal concentration is observed for J_{sc}, which increases from only 0.06 mA/cm^2 for 0 % to 0.18 mA/cm^2 for 40 wt% CdSe. Lower nanoparticle loading below this optimum range leads to a significant decrease in efficiency because the amount of CdSe NCs in P3HT matrix seems to be insufficient to form efficient percolation pathways that minimize hopping distances between CdSe nanoparticles for better electron extraction. However, in the case of higher CdSe amount (60 %), the probability of NC aggregation is high leading

Table 1 Comparison of trap-field-limit voltage (V_{TFL}), current density (J), trap density (N_p) and mobility (μ) of photovoltaic cells based on P3HT:%wt CdSe NCs

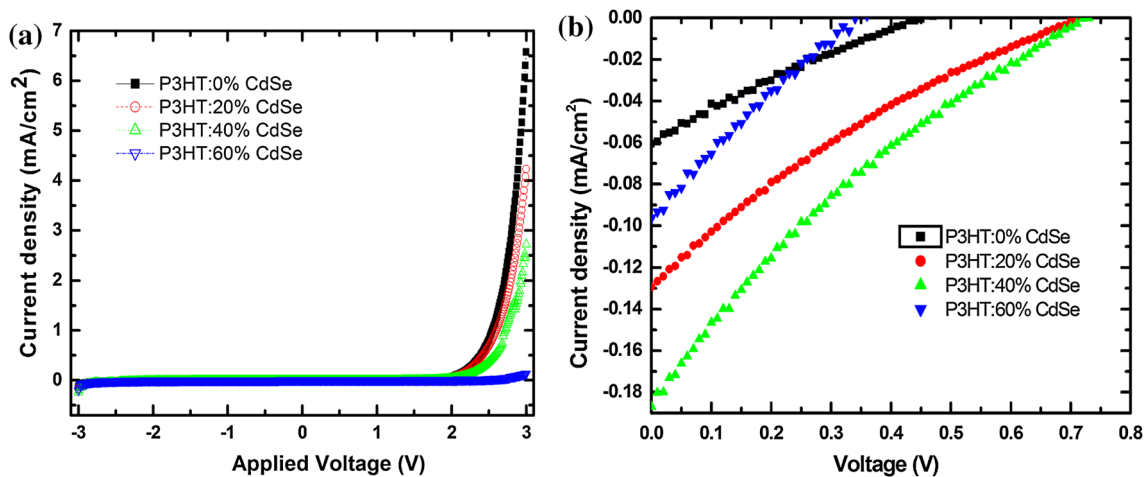| Sample	V_{TFL} (V)	J (μA/cm^2)	N_p (cm^{-3})	μ (cm^2/V/s)
P3HT:0 % CdSe	1.33	9.21×10^{-4}	0.82×10^{16}	1.60×10^{-5}
P3HT:20 % CdSe	1.31	1.13×10^{-3}	0.98×10^{16}	1.42×10^{-5}
P3HT:40 % CdSe	1.30	8.94×10^{-4}	1.06×10^{16}	1.28×10^{-5}
P3HT:60 % CdSe	2.15	8.82×10^{-3}	2.66×10^{16}	5.64×10^{-5}

Fig. 9 Current density voltage (J–V) characteristics of hybrid P3HT:CdSe solar cells measured with different CdSe concentrations: **a** in the dark and **b** under illumination
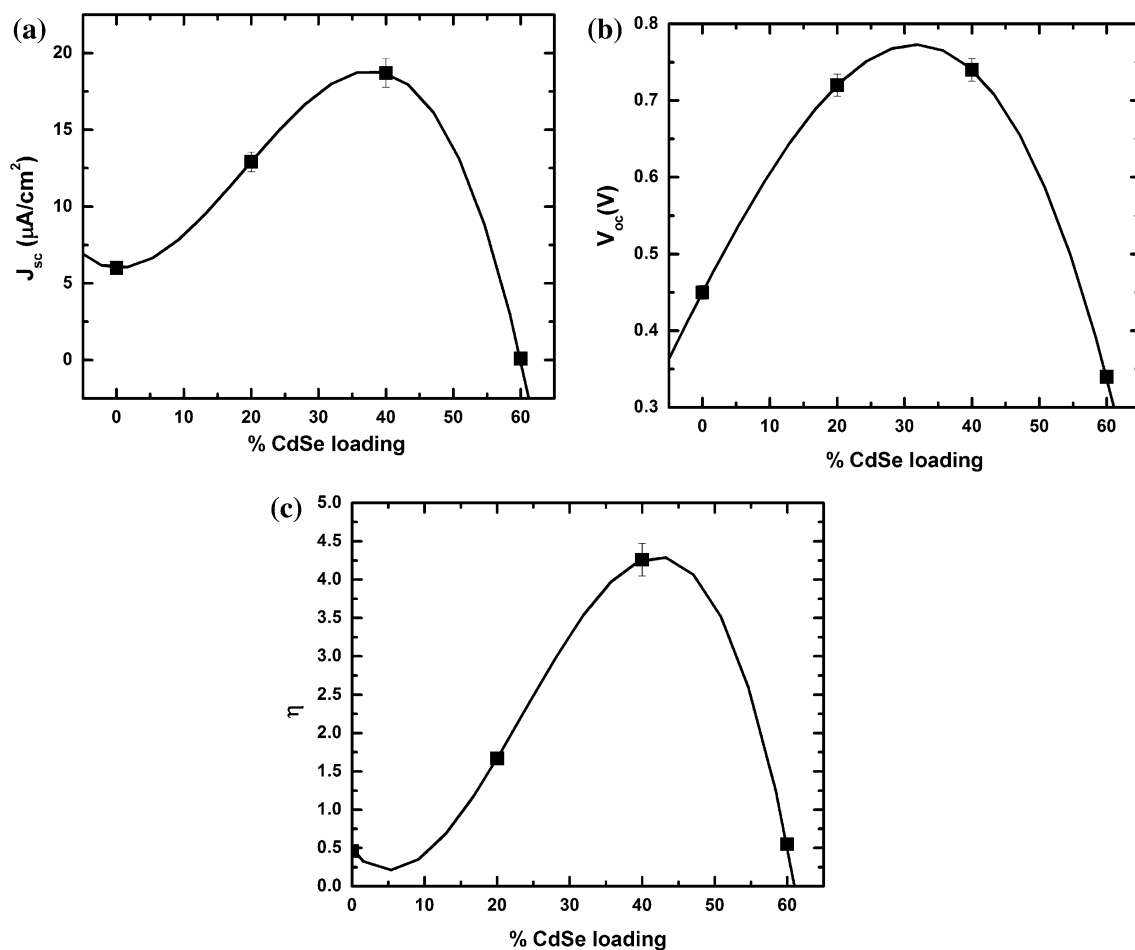

Fig. 10 J–V variation for **a** V_{oc}, **b** J_{sc} and **c** η of devices as a function of CdSe NCs wt% concentration in the blend

to small contact surface P3HT:CdSe and therefore to low exciton dissociation. It is therefore concluded that the optimized sample corresponds to 40 % CdSe, leading to η of 0.25 % with $V_{oc} = 0.74$ V and $J_{sc} = 0.18$ mA/cm². This is in good agreement with optical and structural results described in the previous sections.

Table 3 Series and shunt resistances (in $K/\Omega^{-1}/cm^{-2}$) of P3HT:CdSe composites

	P3HT:0 % CdSe	P3HT:20 % CdSe	P3HT:40 % CdSe	P3HT:60 % CdSe
Series resistance	51	41	30	21
Shunt resistance	27	17	12	14

The low efficiency value can be understood in this term: The low fill factor could be attributed to the organic ligand at the surface of TBPO-capped CdSe NCs and the poor electrical contact with the metallic electrode due to surface roughness [27, 38].

Despite the fact that the fabrication conditions (annealing temperature, active layer thickness, etc.) of our devices are hardly similar to published ones which used TOPO as a capping agent, the closest experimental conditions are those reported by Singh et al. [47]. Their fabricated solar device showed a short-circuit current (J_{sc}) 0.51 mA/cm^2 and open-circuit voltage (V_{oc}) 0.44 V with a maximum conversion efficiency of 0.112 %. As expected, this lower-efficiency solar cell compared to our devices is primarily due to low open-circuit voltage and an expected poor fill factors (FFs).This can be rationalized by considering the insulating nature of the TOPO ligand shell from the high organic content. Considering the smaller TBPO capping agent, our devices based on CdSe(TBPO) acceptors give reasonable efficiencies of $\eta = 0.25$ %. An increase in V_{oc} (0.74 mA/cm^2) and FF (0.19) relative to devices using CdSe(TOPO) acceptors can be explained by the reduced barrier to interfacial charge transfer facilitated by the smaller TBPO ligand shell and overall reduced organic content [18]. Also, Dayal et al. [48] show P3HT:CdSe device efficiency near of our values.

In order to explain the shape of J–V characteristics of our devices and the relatively small fill factor obtained, we have tentatively calculated the shunt and series resistances for the different samples (Table 3). Although the values of these resistances are far from being of physical significance and despite the fact that our devices displayed a poor saturation of current under illumination (Fig. 9b), the calculated resistances show the expected general tendency: The shunt resistance remained practically unchanged when the CdSe concentration was varied between 20 and 60 %, while the series resistance did show a significant reduction from 51 to only 21 $K/\Omega^{-1}/cm^{-2}$ when the CdSe amount was increased from 0 to 60 %, respectively (see Table 3), indicating the key role of CdSe NCs in reducing the difficulty in (dissociation) extracting the charge to the electrodes. However, even at 60 % CdSe, the series resistance remained very large which could be due, among others, to the measured low carrier mobility (1.7×10^{-5} cm^2/V/s) giving accordingly such an S-shaped J–V response, in fair agreement with the organic solar cell circuit model tendency proposed by Mazhari [49].

It is worth noting that the S-shaped J–V characteristics and the poor fill factor of our solar cell systems could also be explained by metal–organic material physical and/or physicochemical interactions and morphology [50] during and after device fabrication as well as to the expected strong interface dipoles [51] described elsewhere.

4 Conclusions

We have studied the optical and electrical properties of hybrid P3HT:CdSe solar cells fabricated with different TBPO-capped CdSe wt% concentrations. This showed that the optimized sample corresponds to 40 wt% CdSe device with photovoltaic parameters of $\eta = 0.25$ with $V_{oc} = 0.74$ V and $J_{sc} = 18.71$ μA/cm^2. The results indicate that capping with TBPO, a moderately bulky and rarely used surfactant did not passivate considerably the CdSe surface and there could be no need for exchange with pyridine process which is commonly used with bulky surfactants such as TOPO. Our results also show that the improvement in the power conversion efficiency of the P3HT:TBPO-CdSe blend at 40 wt% is mainly due to PL quenching.

References

1. Y.H. Lee, D.H. Kim, N.S. Arul, T.W. Kim, Appl. Surf. Sci. **268**, 156–162 (2013)
2. M.C. Scharber, N.S. Sariciftci, Prog. Polym. Sci. **38**, 1929–1940 (2013)
3. Y. Park, D.W. Suh, K.S. Choi, J.S. Yoo, J. Ham, J. Lee, S.Y. Kim, Org. Electron. **14**, 1021–1026 (2013)
4. B. Rand, P. Peumans, S.R. Forrest, J. Appl. Phys. **96**, 7519 (2012)
5. D. Duche, P. Torchio, L. Escoubas, F. Monestier, J.-J. Simon, F. Flory, G. Mathian, Sol. Energy Mater. Sol. Cells **93**, 1377–1382 (2009)
6. M.D. Brown, T. Suteewong, R.S.S. Kumar, V. D'Innocenzo, A. Petrozza, M.M. Lee, U. Wiesner et al., Nano Lett. **11**, 438–445 (2011)
7. A.J. Heeger, J. Phys. Chem. B **105**, 8475–8491 (2001)
8. K.M. Coakley, M.D. McGehee, Chem. Mater. **16**, 4533–4542 (2004)
9. C.B. Murray, D.J. Noms, M.G. Bawendi, J. Am. Chem. Soc. **115**, 8706–8715 (1993)
10. J.L. Birman, N.Q. Huong, J. Lumin. **125**, 196–200 (2007)
11. H. Kim, M. Achermann, L.P. Balet, J.A. Hollingsworth, V.I. Klimov, J. Am. Chem. Soc. **127**, 544–546 (2005)
12. A.J. Moule, L. Chang, C. Thambidurai, R. Vidu, P. Stroeve, J. Mater. Chem. **22**, 2351–2368 (2012)

13. P.D. Cozzoli, T. Pellegrino, L. Manna, Chem. Soc. Rev. **35**, 1195–1208 (2006)
14. M.D. McGehee, MRS Bull. **34**, 95–100 (2009)
15. S.E. Habas, H.A.S. Platt, M.F.A.M. Van Hest, D.S. Ginley, Chem. Rev. **110**, 6571–6594 (2010)
16. T. Xu, Q. Qiao, Energy Environ. Sci. **4**, 2700–2720 (2011)
17. S.N. Sharma, H. Sharms, G. Singh, S.M. Shivaprasad, Mater. Chem. Phys. **110**, 471–480 (2008)
18. Y. Zhou, F.S. Riehle, Y. Yuan, H.F. Schleiermacher, M. Niggemann, G.A. Urban, M. Kruger, Appl. Phys. Lett. **96**, 013304 (2010)
19. S. Dayal, N. Kopidakis, D.C. Olson, D.S. Ginley, G. Rumbles, Nano Lett. **10**, 239–242 (2010)
20. K.F. Jeltsch, M. Schadel, J.B. Bonekamp, P. Niyamakom, F. Rauscher, H.W.A. Lademann, I. Dumsch, S. Allard, U. Scherf, K. Meerholz, Adv. Funct. Mater. **22**, 397–404 (2012)
21. W.F. Fu, Y. Shi, W.M. Qiu, L. Wang, Y.X. Nan, M.M. Shi, H.Y. Li, H.Z. Chen, Phys. Chem. Chem. Phys. **14**, 12094–12098 (2012)
22. M.J. Greaney, S. Das, D.H. Webber, S.E. Bradforth, R.L. Brutchey, ACS Nano **6**, 4222–4230 (2012)
23. Y. Wu, G. Zhang, Nano Lett. **10**, 1628–1631 (2010)
24. N. Radychev, I. Lokteva, F. Witt, J. Kolny-Olesiak, H. Borchert, J.r. Parisi, J. Phys. Chem. C **115**, 14111–14122 (2011)
25. R. Stalder, D. Xie, R. Zhou, J. Xue, J.R. Reynolds, K.S. Schanze, Chem. Mater. **24**, 3143–3152 (2012)
26. J.Y. Lek, L. Xi, B.E. Kardynal, L.H. Wong, Y.M. Lam, A.C.S. Appl, Mater. Interfaces **3**, 287–292 (2011)
27. X.X. Jiang, F. Chen, W.M. Qiu, Q.X. Yan, Y.X. Nan, H. Xu, L.G. Yang, H.Z. Chen, Sol. Energy Mater. Sol. Cells **94**, 2223–2229 (2010)
28. F. Teng, A. Tang, B. Feng, Z. Lou, Appl. Surf. Sci. **254**, 6341–6345 (2008)
29. J.J. Tauc, Non-Cryst Solids **149**, 97–98 (1987)
30. T. Trindade, P. O'Brien, Chem. Mater. **9**, 523–530 (1997)
31. E. Campos-Gonzalez, P. Rodriguez-Fragozo, G. Gonzalez de la Cruz, J. Santoyo-Salazar, O. Zelaya-Angel, J. Cryst. Growth **338**, 251–255 (2012)
32. A. Manna, R. Bhattacharya, T.K. Das, S. Saha, Phys. B **406**, 981–984 (2011)
33. D.E. Motaung, G.F. Malgas, C.J. Arendse, S.E. Mavundla, C.J. Olophant, D. Knoesen, J. Mater. Sci. **44**, 3192 (2009)
34. N.T.N. Truong, W.K. Kim, U. Farva, X.D. Luo, C. Park, Sol. Energy Mater. Sol. Cells **95**, 3009–3014 (2011)
35. A. Bruno, T. Di Luccio, C. Borriello, F. Villani, S.A. Haque, C. Minarini, Energy Procedia **44**, 167–175 (2014)
36. N.C. Greenham, X. Peng, A.P. Alivisatos, Phys. Rev. B **54**, 17628–17637 (1996)
37. S.N. Sharm, T. Vats, N. Dhenadhayalan, P. Ramamurthy, A.K. Narula, Sol. Energy Mater. Sol. Cells **100**, 6–15 (2012)
38. A. Benchaabane, Z. Ben Hamed, F. Kouki, A. Zeinert, H. Bouchriha, Appl. Phys. A **120**, 1149–1157 (2015)
39. Z. BenHamed, N. Mastour, A. Benchaabane, F. Kouki, M.A. Sanhoury, H. Bouchriha, J. Lumin. **170**, 30–36 (2016)
40. J. Yang, A. Tang, R. Zhou, J. Xue, Sol. Energy Mater. Sol. Cells **95**, 476–482 (2011)
41. J. Sworakowski, G.F. Leal Ferreira, J. Phys. D Appl. Phys. **17**, 135–139 (1984)
42. A.V. Nenashev, M. Wiemer, F. Jansson, S.D. Baranovskii, J. Non-Cryst. Solids **358**, 2508–2511 (2012)
43. A. Benchaabane, Z. Ben Hamed, F. Kouki, M.A. Sanhoury, K. Zellama, A. Zeinert, H. Bouchriha, J. Appl. Phys. **115**, 134313 (2014)
44. J. Bisquert, A. Zaban, M. Greenshtein, I. Mora-Sero, J. Am. Chem. Soc. **126**, 13550–13559 (2004)
45. C. Goh, R. Joseph Kline, M.D. McGehee, Appl. Phys. Lett. **86**, 122110 (2005)
46. M.S. Ryu, J. Jang, Sol. Energy Mater. Sol. Cells **95**, 3015–3020 (2011)
47. V.K. Verma, Y. Singh, R.N. Chauhan, R.S. Anand, J. Kumar, Integr. Ferroelectr. **120**, 1–5 (2010)
48. S. Dayal, M.O. Reese, A.J. Ferguson, D.S. Ginley, G. Rumbles, N. Kopidakis, S. Cells, Adv. Funct. Mater. **20**, 2629–2635 (2010)
49. B. Mazhari, Sol. Energy Mater. Sol. Cells **90**, 1021–1033 (2006)
50. D. Gupta, M. Bag, K.S. Narayan, Appl. Phys. Lett. **92**, 093301 (2008)
51. A. Kumar, S. Sista, Y. Yang, J. Appl. Phys. **105**, 094512–094516 (2009)